Journal of Materials Chemistry B

PAPER

View Article Online
View Journal | View Issue

Cite this: J. Mater. Chem. B, 2018, 6, 1995

Hierarchical theranostic nanomedicine: MRI contrast agents as a physical vehicle anchor for high drug loading and triggered on-demand delivery†

Guangqin Liu, ‡[a] Jian Deng, ‡[a] Fang Liu, [a] Zheng Wang, [ab] Dan Peer [c] and Yanjun Zhao *[a]

Received 16th January 2018,
Accepted 5th March 2018

DOI: 10.1039/c8tb00135a

rsc.li/materials-b

The loading of drugs and imaging agents in theranostic nanomedicines by a physical approach is usually poor (<5%), which limits their therapeutic effect and translation potential. We report a hierachical hybrid nanocarrier made of a manganese phosphate core, an outermost lipid shell, and an electrostatically deposited campothecin phosphonate interfacial middle layer. The hydrophobic interactions between camptothecin and lipid layers maintained the integrity and stability of the hybrid nanocarrier. Such a nanoplatform could surprisingly load camptothecin over 15% (w/w) with decent serum stability. The nanocarrier displayed pH-dependent cargo release profiles due to particle collapse under acidic conditions under which the r_1 relaxivity of magnetic resonance imaging (MRI) was 25.2 mM^{-1} s^{-1} (pH 5.0). The nanocarrier could efficiently transport camptothecin into 4T1 cells with a half maximal inhibitory concentration of 5.4 ± 0.3 μM. Both *in vivo* MRI and fluorescence imaging analysis revealed that the nanocarrier could competently deliver the cargo to the tumor site. The anticancer efficacy of camptothecin-loaded nanocarrier was proved using the same 4T1 tumor-bearing mice model coupled with the histological and apoptosis analysis. This work not only presented a novel drug encapsulation approach, but also provided a new theranostic hybrid nanoplatform which could realize MRI-guided delivery of hydrophobic agents.

Introduction

Multifunctional nanomedicine holds great value in treating a diverse range of diseases.[1,2] Efficient and ratiometric cargo loading in nanocarriers together with on-demand release is essential to fulfil the mission of nanotechnology in biomedicine, which is particularly valid when the cargo potency is low.[3–5] However, cargo encapsulation in nanocarriers (*e.g.* liposomes, micelles, dendrimers, polymer nanoparticles) by traditional physical means is very poor; the drug loading is typically less than 5% (w/w).[6] The fundamental reason for this phenomenon is the lack of sufficient carrier–drug affinity and the limited void space in the nanocarrier to retain the drugs. The forces holding the drugs within the nanocarrier (*e.g.* hydrophobic interactions, hydrogen bonding, van der Waals forces, and electrostatic interactions) are often non-specific, *i.e.* they also exist between free drug molecules, leading to drug aggregation and precipitation.[6] Efforts have been continuously devoted to address the loading issue in nanocarriers. Wei *et al.* reported an amphiphilic dendrimer with a large void space that can reach a drug loading of over 40%.[7] Cai *et al.* developed a dimeric drug nanoparticle with a high loading (>50%) *via* inhibiting drug crystallization.[8] The amphiphilic prodrug and drug–drug conjugate is another popular means for loading improvement.[9–11] Engineering pure drug nanocrystals is also a smart method to enhance loading.[12] Liu *et al.* utilized superfast sequential microfluidic nanoprecipitation and produced a drug nanocrystal core–polymer shell nanocarrier with a high loading.[13] Nevertheless, when it comes to the loading of multiple agents (*e.g.* an imaging agent and a drug), a robust and efficient loading method is still required.

Regarding the efficient cargo loading in theranostic nanocarriers, Hollis *et al.* developed paclitaxel nanocrystals with a

[a] School of Pharmaceutical Science & Technology, Tianjin Key Laboratory for Modern Drug Delivery & High Efficiency, and Collaborative Innovation Center of Chemical Science and Engineering (Tianjin), Tianjin University, Tianjin 300072, China. E-mail: zhaoyj@tju.edu.cn
[b] Stake Key Laboratory of Medicinal Chemical Biology, Nankai University, Tianjin 300071, China
[c] Laboratory of Precision NanoMedicine, Department of Cell Research & Immunology, George S. Wise Faculty of Life Sciences, Department of Materials Sciences and Engineering, Iby and Aladar Fleischman Faculty of Engineering, Center for Nanoscience and Nanotechnology, and Cancer Biology Research Center, Tel Aviv University, Tel Aviv 69978, Israel

† Electronic supplementary information (ESI) available. See DOI: 10.1039/c8tb00135a

‡ These authors contributed equally to this work.

fluorescent probe embedded within the crystal lattice.[14] The crude design might be only valid for a small group of compounds that display unique physicochemical properties (*e.g.* high hydrophobicity). In addition, drug release from these nanocrystals is mainly driven by a dissolution mechanism, which is usually very slow and a delayed onset of action is expected. Recently, manganese (Mn^{2+}) was reported to be co-precipitated in lipid-calcium phosphate (LCP) nanocarriers to realize magnetic resonance imaging (MRI).[15] LCP is usually composed of an inorganic calcium phosphate core and an asymmetric lipid bilayer shell; the core and shell are united *via* the electrostatic interaction at the core–shell interface.[16] Moreover, LCP inherently displays a triggered release characteristic; upon cellular uptake *via* endocytosis, the cargo in the core can be released post particle collapse within the acidic endosome/lysosome.[17]

Inspired by the structure of LCP, we postulated that manganese phosphate (MnP) nanoparticles could be used as an anchor to interfacially deposit negatively charged drugs by electrostatic interactions (Scheme 1). The combination of large surface area of nanoparticles and electrostatic interactions would ensure a high loading without premature dose dumping. The acid-labile disintegration of MnP could enable intracellular on-demand release. Many drugs contain ionic groups (*e.g.* phosphonate) or can be easily engineered to obtain a phosphonate moiety, which means that this approach is robust and applicable to a large collection of drugs. The manganese dose can be readily manipulated by calcium doping; hence the ratio of imaging agents and drugs can be precisely regulated. Hence, the aim of this study was to employ a novel "drug encapsulation by imaging agents" approach to engineer high drug loading theranostic MRI nanomedicine with pH-triggered delivery properties. The cationic MnP core was coated with ionic drugs *via* interfacial electronic deposition, followed by lipid coating to generate a hierarchical hybrid nanocarrier. Camptothecin (CPT) was modified and used as the model drug.

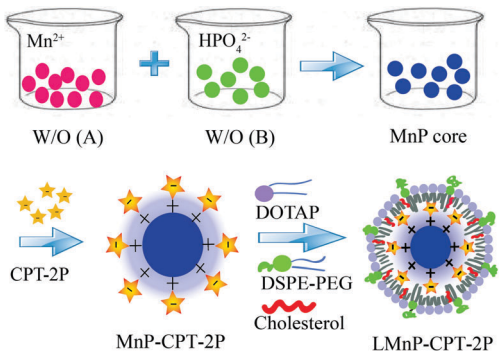

Scheme 1 Illustrative production of lipid-manganese phosphate (LMnP) hybrid nanocarriers with the model drug interfacially deposited onto the core surface. First, manganese and hydrogen phosphate were incorporated into the internal phases of two water-in-oil microemulsions, respectively. The mixing of two microemulsions generated solid manganese phosphate (MnP) particles as the anchor for drug loading. Then the model drug, camptothecin (CPT) was modified to produce a diphosphonate-containing derivative (CPT-2P) before electronically deposited onto the surface of the MnP core, generating a MnP-CPT-2P nanocarrier. After surface coating with various lipids (DSPE-PEG, DOTAP, and cholesterol), the hybrid nanocarrier was obtained (*i.e.* LMnP-CPT-2P). MRI indicates magnetic resonance imaging.

Results and discussion

Preparation and characterization of hybrid nanocarriers

CPT contains one hydroxyl group that is utilized to attach the phosphate moiety. Two camptothecin derivatives, *i.e.* camptothecin monophosphonate (CPT-P) and camptothecin diphosphonate (CPT-2P), were successfully synthesized with one (CPT-P) or two (CPT-2P) phosphate groups being covalently conjugated *via* esterification, respectively (Scheme S1 and Fig. S1–S6, ESI†). CPT-P or CPT-2P together with the standard middle lipid layer of LMnP, dioleoylphosphatidic acid (DOPA), was co-deposited on the surface of MnP at five different molar supplementation ratios. As expected, both types of CPT derivatives can be effectively loaded in the hybrid nanocarriers. Regarding CPT-P, the drug content in the hybrid nanocarriers increased with elevated portion of CPT-P in the feeding mixture; the particle size of the obtained nanocarriers also increased accordingly when more CPT was present at the MnP surface (Fig. S7, ESI†). A similar trend was observed for CPT-2P; nevertheless, the drug loading was much higher, reaching 16.9 ± 3.0% (w/w) when no DOPA lipid is present (Fig. 1A).

The high drug loading is surprising as the typical drug content in nanoparticles *via* physical encapsulation is less than 5% (w/w).[18] The strategies of creating void spaces within particles or inhibiting drug precipitation *via* dimer formation

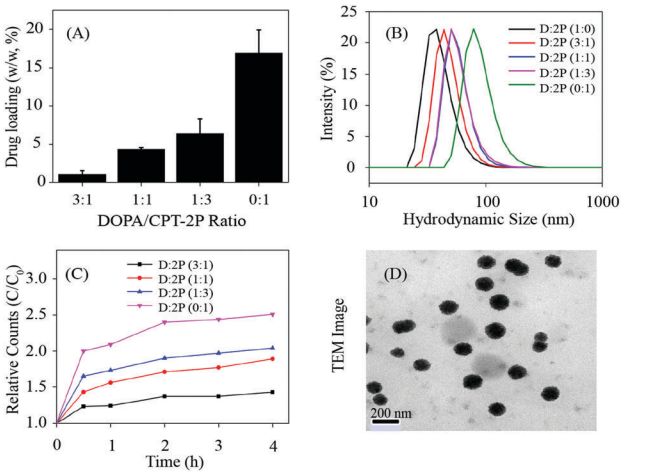

Fig. 1 Physiochemical properties of hybrid nanocarriers with different compositions in the middle layer. (A) The drug loadings in the hybrid nanocarrier when mixtures of dioleoylphosphatidic acid (DOPA) and a model drug camptothecin diphosphonate (CPT-2P) with different molar ratios were supplemented for the particle fabrication; (B) the hydrodynamic sizes of various hybrid nanocarriers that differed in DOPA and CPT-2P ratio (*i.e.* D : 2P) during manufacture; (C) the serum stability of hybrid nanocarriers that differed in DOPA and CPT-2P ratio; (D) the transmission electron microscopy (TEM) image of hybrid nanocarriers (LMnP-CPT-2P) in the absence of DOPA.

were reported previously to increase physical drug loading.[19,20] In contrast to these methods, high drug loading is simply achieved by interfacial electrostatic deposition in the current work. It is reasonable that nanocarriers containing CPT-2P display a higher loading than their counterparts containing CPT-P. As a consequence of the elevated charge density of CPT-2P compared to its counterpart CPT-P, CPT-2P would display a greater degree of electrostatic interaction with MnP to secure a high drug loading. The fact that particle size became larger when more CPT is deposited onto the MnP core was presumed to be due to the dissimilar packing mode of CPT compared to DOPA, as well as the altered interactions between the outer layer lipids and middle layer components (CPT or DOPA) (Fig. 1B). Irrespective of the CPT type, the hybrid nanocarriers displayed similar hydrodynamic size at a fixed CPT/DOPA feeding ratio (Fig. 1B and Fig. S7, ESI†). The zeta potential of LMnP-CPT-2P was -15.3 ± 0.8 mV (without lipid coating) and 14.0 ± 1.9 mV (with lipid layer), respectively.

The serum stability of the (CPT-2P)-loaded hybrid nanocarrier was determined by utilizing the inherent fluorescence of CPT based on a previously reported method.[21] The increase of fluorescence upon incubation indicates the release of CPT because the fluorescence will be quenched to a certain extent due to the aggregation caused quenching effect when the drug is crowded at the MnP surface. All types of investigated nanocarriers showed a time-dependent increase of CPT fluorescence, suggesting the release of some CPT. The stability curve of nanocarriers with a high CPT loading ranked beyond those with relatively low CPT content. However, all curves almost got plateaued after one hour, indicating the relative stability of these particles (Fig. 1C). Therefore, the DOPA-free hybrid nanocarrier (*i.e.* the highest CPT loading, abbreviated as LMnP-CPT-2P) was selected for further drug release study and investigation on the cellular and animal models. Transmission electron microscopy images revealed that LMnP-CPT-2P nanocarriers displayed a spherical shape with a nanoscale diameter (Fig. 1D and Fig. S8, ESI†). The corresponding TEM size of the LMnP core was *ca.* 10 nm (Fig. S9, ESI†).

Drug release and *in vitro* MRI assessment

The *in vitro* drug release was performed at a physiological temperature (37 °C) under two pH conditions (7.4 or 5.0). The former mimics the neutral blood circulation, while the latter reflects the acidic endosomes and lysosomes (down to pH 4.5).[22] The hybrid nanocarriers demonstrated a distinctive pH-dependent release profile for both CPT and Mn^{2+} (Fig. 2A–B). At low pH (5.0), the rate and extent of cargo release was significantly higher than that at pH 7.4. This phenomenon concurred well with previous reports on drug release from LCP nanocarriers.[15,16,23] As a polyprotic acid, there are three disassociation constants related to the phosphate group (pK_{a1} = 2.1, pK_{a2} = 7.2, and pK_{a3} = 12.7). Under neutral conditions (pH 7.4), hydrogen phosphate (HPO_4^{2-}) is the major species (pH > pK_{a2}), which enables their anchoring with Mn^{2+} to maintain the integrity of hybrid particles. When pH was reduced well below its pK_{a2}, the dihydrogen phosphate ($H_2PO_4^-$) predominates, resulting in a decrease in the electrostatic

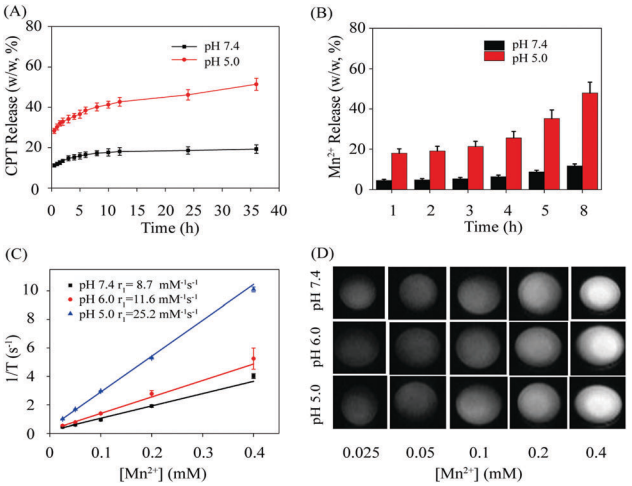

Fig. 2 *In vitro* drug release and magnetic resonance imaging analysis of LMnP-CPT-2P hybrid nanocarriers. (A) Cumulative release of the model drug (camptothecin/CPT) under two different pH conditions (7.4 and 5.0); (B) cumulative manganese (Mn^{2+}) release under the neutral and acidic conditions (pH 7.4 and 5.0); (C) the r_1 relaxivity plot of hybrid nanocarriers under three different pH conditions (7.4, 6.0, and 5.0); (D) the T_1-weighted magnetic resonance images of hybrid nanocarriers under the same three pH conditions (7.4, 6.0, and 5.0).

interaction between Mn^{2+} and the phosphoric anions, gradual disassembly of hybrid nanocarriers, and hence cargo liberation. Since the tertiary amine in CPT-2P exhibits a higher pK_a (>10), it should remain fully ionized at both pH 7.4 and pH 5.0. Therefore, this group would not affect the drug release profile. As CPT-2P showed decent water solubility, the free CPT-2P dissolved in water medium in a nano-suspension could rapidly transport across the membrane, leading to a release curve that didn't start from zero at the vertical axis.

As estimated, the hybrid nanocarrier displayed the capability for T_1-weighted MRI *in vitro* (Fig. 2C and D). The calculated r_1 relaxivity increased dramatically with the reduction of the medium pH and the highest r_1 obtained was 25.2 mM^{-1} s^{-1} at pH 5.0. These data can be easily explained by the rapid Mn^{2+} release kinetics under more acidic conditions (Fig. 2B). The employment of manganese-containing nanocarriers has been reported as an alternative to gadolinium-based contrast agents to realize T_1-weighted MRI.[24,25] Particularly, the released Mn^{2+} can bind with surrounding proteins and hence increase the spin–lattice relaxation, leading to enhanced contrast and an amplified signal.[14] The manganese in the hybrid nanocarrier not only functions as a MRI contrast agent, but also acts as the particle building block to interfacially load the drug between the inorganic core and the outermost lipid shell.

Cytotoxicity and cellular uptake

The free CPT-2P showed a much lower cytotoxicity (IC_{50} = 6.4 ± 1.0 μM) compared to its unmodified counterpart (CPT, IC_{50} = 3.9 ± 0.3 μM) ($p < 0.05$) (Fig. 3A and Table S1, ESI†), which was believed to be a result of its poor cellular uptake since both CPT-2P and cell membranes were negatively charged. Upon being loaded in the hybrid nanocarriers, the charge of CPT-2P

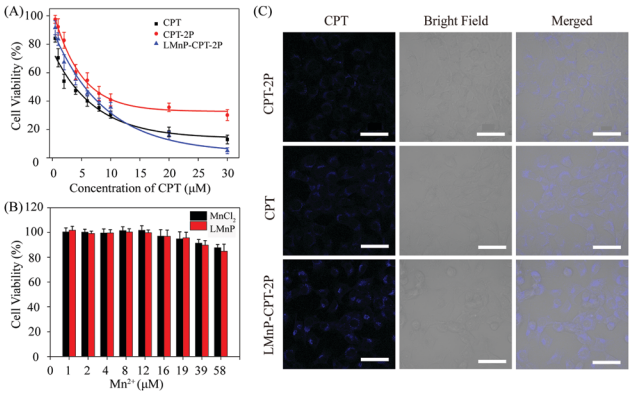

Fig. 3 Cellular uptake and potency analysis of hybrid nanocarriers in 4T1 cells. (A) Dose-dependent cell viability of 4T1 cells in response to the LMnP-CPT-2P nanocarrier and two controls: camptothecin (CPT) and camptothecin diphosphonate (CPT-2P); (B) dose-dependent cell viability of 4T1 cells in response to the drug-free nanocarrier (LMnP) and the control ($MnCl_2$); (C) intracellular uptake of the LMnP-CPT-2P nanocarrier, free CPT, and CPT-2P. Scale bar: 50 μm.

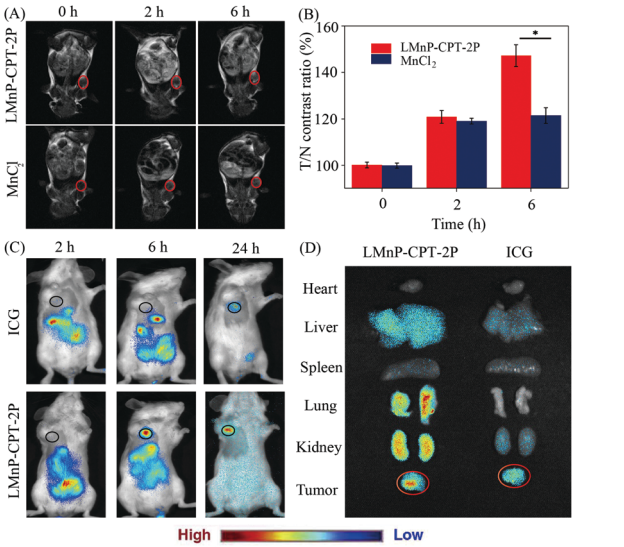

Fig. 4 *In vivo* MRI and fluorescent images of 4T1 tumor-bearing mice at different time points post intravenous injection of LMnP-CPT-2P hybrid nanocarriers and the corresponding controls. (A) T_1-Weighted MRI images of LMnP-CPT-2P against $MnCl_2$ control at 0 h, 2 h and 6 h post dose administration; (B) semi-quantitative analysis of MRI signals from the tumor and normal tissues (T/N contrast) (n = 3); (C) fluorescent images of whole animal at 2 h, 6 h and 24 h post administrating the indocyanine green (ICG)-loaded LMnP-CPT-2P nanocarrier or free ICG control; (D) fluorescent images of the tumor and major healthy organs 24 post dose administration. Circles represent the tumor location; *$p < 0.05$.

was neutralized and the endocytosis-mediated particle uptake could carry the drug to the intracellular environment. The cytotoxicity of the hybrid nanocarrier (IC_{50} = 5.4 ± 0.3 μM) potentially arose from two parts: CPT-2P and Mn^{2+}. Once being transported into cells, CPT-2P should be converted to CPT *via* intracellular esterase before binding to the target (*i.e.* DNA topoisomerase I). To examine the effect of Mn^{2+} on the cell viability, a LMnP control nanocarrier in the absence of CPT was prepared with DOPA as the middle layer. The manganese loading was 5.2 ± 0.8% (w/w, LMnP-CPT-2P) and 8.6 ± 0.9% (w/w, LMnP), respectively. The maximum manganese dose (*ca.* 58 μM) in LMnP was set to be identical to that of LMnP-CPT-2P in which the CPT concentration was 30 μM. The cell viability assay showed no cytotoxicity of Mn^{2+} within the investigated dose range with free Mn^{2+} ($MnCl_2$) as the control (Fig. 3B). Several independent studies have previously revealed that Mn^{2+} only exerted apparent cytotoxicity at a dose larger than 100 μM.[15,26,27] Hence, the contribution of Mn^{2+} to cell viability could be neglected in Fig. 3A. Confocal laser scanning images demonstrated that the extent of drug uptake ranked as follows: nanocarrier > free CPT > free CPT-2P (Fig. 3C and Fig. S10, ESI†). Such a ranking was a consequence of electrostatic repulsion between the free drugs with a negatively charged cell membrane, resulting in limited cellular uptake. Although more drugs were internalized with the aid of the nanocarrier, CPT-2P must be released from the carrier and converted back to CPT before exerting the therapeutic action. Hence, free CPT as a positive control still showed higher cytotoxicity than the hybrid nanocarriers.

In vivo and *ex vivo* imaging

The LMnP-CPT-2P hybrid nanocarriers displayed good biocompatibility, as supported by the low hemolysis degree (0.7 ± 0.2%, n = 3). The drug-free nanocarrier (LMnP) and free drug (CPT-2P) are also not hemolytic with a corresponding hemolysis extent at 0.7 ± 0.1% (LMnP) and 0.8 ± 0.1% (CPT-2P). Since both nanocarriers are surface-coated with biocompatible lipids, these results are sensible. The kinetic tumor distribution of hybrid nanocarriers *in vivo* was realized by MRI with $MnCl_2$ as the control (Fig. 4A, B and Fig. S11, ESI†). A murine 4T1-bearing model was employed.[28] Regarding the LMnP-CPT-2P nanocarrier, the highest manganese level in the tumor was observed 6 h post intravenous dose administration. In terms of the control, there was not much difference between the signals at 4 h and at 6 h. In contrast, at 6 h post dose delivery, the MRI signal from the nanocarrier was significantly higher than that of the control ($MnCl_2$) ($p < 0.05$). This was believed to be a consequence of the enhanced permeability and retention (EPR) effect that usually reached the peak *ca.* 6 hours post dose administration.[29,30] The biodistribution of LMnP-CPT-2P hybrid nanocarriers was also analyzed with the aid of a near infrared fluorescent probe, indocyanine green (ICG) that was encapsulated within the inorganic core. In good agreement with *in vivo* MRI data, the fluorescence analysis demonstrated a peak intensity of ICG at 6 h post dose administration (Fig. 4C and D); there was no such trend for the control sample (free ICG). Similarly, this was also a consequence of the EPR effect. At 24 h post administration, the ICG amount in the tumor was much higher than that of the control, indicating the good ability for targeted tumor delivery.

In vivo efficacy

The *in vivo* efficacy study was performed in 4T1 tumor-bearing mice models. In contrast to the controls including PBS, free CPT-2P, and LMnP nanocarrier, the hybrid nanocarrier (LMnP-CPT-2P) displayed

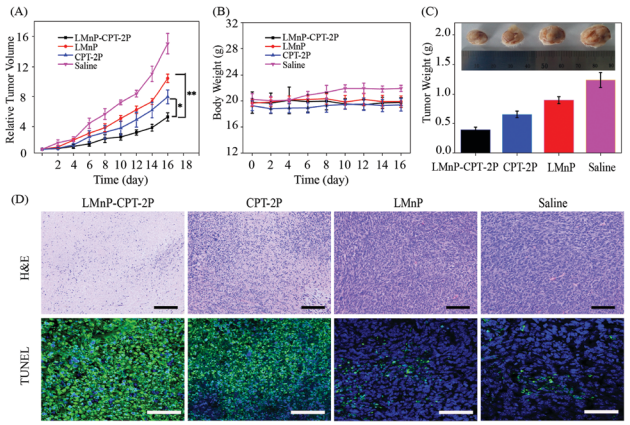

Fig. 5 *In vivo* antitumor efficacy of LMnP-CPT-2P hybrid nanocarriers with three controls: drug-free nanocarrier (LMnP), free CPT-2P, and saline. (A) The tumor growth inhibition curve post intravenous administration; (B) mice body weight variation during the treatment course; (C) representative images and average weight of excised tumor at the end of the efficacy study; (D) histological (H&E) and TUNEL staining of tumor tissues post efficacy study. All data were presented as the mean ± standard deviation (n = 6). Scale bar: 100 μm (H&E); 50 μm (TUNEL); *$p < 0.05$, **$p < 0.01$.

the best anti-cancer performance, as indicated by the extent of tumor growth inhibition (Fig. 5A and C). At the end of the efficacy study, there was a significant difference between the degrees of tumor inhibition between LMnP-CPT-2P and CPT-2P ($p < 0.05$), and between LMnP-CPT-2P and LMnP ($p < 0.01$). It was interesting that CPT-free LMnP nanocarriers also displayed certain anti-tumor effect, which might be due to the sufficient accumulation of manganese in the tumor site above the toxicity threshold. Another possible reason is from the toxic effect of cationic lipids at the outermost layer of hybrid carriers since positively charge lipids can induce dose-dependent toxicity.[31] The efficacy data concurred well with the biodistribution results. Since the nanocarriers can deliver more drugs to the tumor site due to the EPR effect, it is rational that free CPT-2P showed inferior ability in inhibiting tumor growth compared to the hybrid nanocarrier, which is analogous to other carrier-mediated anticancer investigations.[32] The mice body weight maintained almost constant for all other three samples except for PBS control, which was a consequence of dramatically uncontrolled tumor growth (Fig. 5B). At the end of the efficacy study, the tumor tissues were analyzed by the histological hematoxylin and eosin (H&E) staining and terminal deoxynucleotidyl transferase dUTP nick end labeling (TUNEL) assay (Fig. 5D). These images were a good reflection of tumor growth inhibition curves. Among all the H&E stained images, the amount of intact nuclei ranked at the bottom for the LMnP-CPT-2P nanocarrier due to its superior anti-cancer effect compared to the other three formulations. It also demonstrated the strongest capability in initiating apoptosis, as evidenced by the highest fluorescence intensity in TUNEL assay images.

Conclusions

A novel interfacial deposition method was presented in a model manganese phosphate–lipid hybrid nanocarrier. Such a nanocarrier could be a robust theranostic nanocarrier for delivery of hydrophobic agents. As many drugs have conjugate sites (*e.g.* hydroxyl, carboxyl, amine), upon being attached with the phosphate moiety, these drugs could be efficiently encapsulated within the middle layer of the hybrid nanocarrier with a decent loading. The manganese content could be easily manipulated by replacing with calcium to balance the MRI ability and toxicity. Such a nanoplatform also provides a strategy for combinational delivery of hydrophilic and hydrophobic agents, as well as small molecule drugs with genes.[33,34] The current work created a method of electronic interfacial deposition for efficient hydrophobic drug loading in hybrid nanocarriers and added new members to the family of multifunctional theranostic nanomedicine.

Experimental section

Materials

Camptothecin (CPT) and branched polyoxyethylene nonylphenyl-ether (Igepal CO-520) were sourced from HWRK Chem Co., Ltd (Beijing, China). 1,2-Dioleoyl-3-trimethylammonium-propane chloride salt (DOTAP), dioleoylphosphatidic acid (DOPA) and cholesterol were purchased from Avanti Polar Lipids, Inc. (Alabaster, AL, USA). 1,2-Distearoyl-*sn-glycero*-3-phosphoethanolamine-*N*-[methoxy(polyethyleneglycol)-2000] ammonium salt (DSPE-PEG2000) was provided by Ponsure Biotechnology (Shanghai, China). Ethanol and cyclohexane were obtained from J&K Scientific Ltd, (Beijing, China). Manganese chloride, *N*,*N*-bis (phosphonomethyl) glycine and 3-phosphonopropanoic acid were obtained from Meryer Chemical Technology Co., Ltd (Shanghai, China). Indocyanine green (ICG), 4-dimethylaminopyridine (DMAP) and 1-(3-dimethylaminopropyl)-3-ethylcarbodiimide hydrochloride (EDCI) were purchased from InnoChem Science & Technology Co., Ltd (Beijing, China). Ethylenediaminetetraacetic acid disodium salt, dichloromethane (DCM), methanol, hydrochloric acid (HCl), tetrahydrofuran (THF), disodium hydrogen phosphate, sodium bicarbonate and normal saline were purchased from Concord Technology Co., Ltd (Tianjin, China). Deuterated water was obtained from Jinouxiang Science & Technology Co., Ltd (Beijing, China). Certified fetal bovine serum was purchased from Biolnd (Cromwell, USA). Dulbecco's Modified Eagle's medium (DMEM), penicillin, streptomycin, and trypsin were from HyClone Inc. (Logan City, Utah, USA). 3-(4,5-Dimethyl-2-thiazolyl)-2,5-diphenyl-2-*H*-tetrazolium bromide (MTT) was obtained from United Stars Biotechnology Co., Ltd (Tianjin, China). 4% paraformaldehyde was purchased from Solarbio Science Technology Co., Ltd (Beijing, China). All other chemicals were sourced from Jiangtian Fine Chemical Research (Tianjin, China).

Synthesis of camptothecin monophosphonate (CPT-P)

The synthesis of camptothecin involves an esterification reaction (Scheme S1, ESI†). In brief, EDCI (2.2 g, 11.38 mmol), DMAP (1.49 g, 12.19 mmol) and 3-phosphonopropionic acid (0.5 g, 3.25 mmol) were dissolved in dichloromethane (30 mL) in a 100 mL round-bottomed flask equipped with a magnetic flea. The mixture was maintained at 30 °C for 1.5 h with nitrogen protection until a

yellow transparent solution was obtained. Camptothecin (0.57 g, 1.62 mmol) dissolved in dichloromethane (10 mL) was then supplemented to the above solution and the obtained mixture was maintained at 30 °C. After constant stirring for 3 days, the solvent was condensed under reduced pressure. Subsequently, the obtained crude product was sealed in a cellulose tube with a molecular weight cut-off (MWCO) of 500 Da that was sequentially dialyzed against an aqueous solution of 0.1 M HCl, an aqueous solution of 1 M sodium bicarbonate, and then deionized water. In the end, the dialysate was passed through a 0.45 μm filter membrane and the recovered solution was lyophilized to obtain camptothecin phosphate (CPT-P) (0.9 g, 93.6% yield), the product was characterized by MS, ^{1}H NMR, and ^{31}P NMR. ^{1}H NMR (400 MHz, D_2O, ppm): δ 1.03 (t, 3H), 1.73 (m, 2H), 2.22 (t, 2H), 2.80 (t, 2H), 5.43 (s, 2H), 5.52 (s, 2H), 7.15 (s, 1H), 7.16 (t, 1H), 7.37 (d, 1H), 7.47 (t, 1H), 7.69 (d, 1H), 7.87 (s, 1H) (Fig. S1, ESI†). ^{31}P NMR (162 MHz, D_2O, ppm): δ 19.58 (Fig. S2, ESI†). ESI-MS in methanol: *m*/*z* (calculated) = 529.07, *m*/*z* (observed) = 529.07 $[M + H]^+$ (Fig. S3, ESI†).

Synthesis of camptothecin diphosphonate (CPT-2P)

The synthesis of CPT-2P employed a similar method. EDCI (0.51 g, 2.66 mmol), DMAP (0.35 g, 2.85 mmol) and *N*,*N*-bis (phosphonomethyl) glycine (0.2 g, 0.76 mmol) were mixed in dichloromethane (30 mL) and maintained at 30 °C for 1.5 h in a nitrogen atmosphere to obtain a yellowish transparent solution. Camptothecin (0.15 g, 0.38 mmol) dissolved in dichloromethane (10 mL) was subsequently added to the above mixture, followed by continuous stirring for 3 days at 30 °C. After the solvent was removed under vacuum, the obtained crude product was sealed in a cellulose tube with MWCO of 500 Da that was sequentially dialyzed against an aqueous solution of 0.1 M HCl, an aqueous solution of 1 M sodium bicarbonate, and then deionized water. Finally, the dialysate was passed through a 0.45 μm filter membrane and the recovered solution was lyophilized to obtain CPT-2P as a pale yellow spongy powder (0.15 g, 81.5% yield); the product was characterized by MS, ^{1}H NMR, and ^{31}P NMR. ^{1}H NMR (400 MHz, D_2O, ppm): δ 1.05 (t, 3H), 2.23 (m, 2H), 2.99 (s, 2H), 3.34 (s, 2H), 4.02 (s, 1H), 4.08 (s, 1H), 5.46 (s, 2H), 5.56 (s, 2H), 7.27 (s, 1H), 7.30 (t, 1H), 7.53 (d, 1H), 7.59 (t, 1H), 7.85 (d, 1H), 8.04 (s, 1H) (Fig. S4, ESI†). ^{31}P NMR (162 MHz, D_2O, ppm): δ 18.66. (Fig. S5, ESI†). ESI-MS in methanol: *m*/*z* (calculated) = 682.02, *m*/*z* (observed) = 682.02 $[M + H]^+$ (Fig. S6, ESI†).

Preparation of hybrid nanocarriers

The production of hybrid nanocarrier employed a previously reported water-in-oil microemulsion method with a minor modification.[16] The first type of microemulsion was obtained by dispersing 150 μL of 2.5 M $MnCl_2$ (pH 7.0) in a 5 mL cyclohexane phase with Igepal CO-520 as the surfactant (cyclohexane: Igepal CO-520 = 71/29, v/v). The second type of microemulsion contained 150 μL of 12.5 mM Na_2HPO_4 (pH 9.0), 5 mL of cyclohexane, and 300 μL of DOPA/CPT-P (or CPT-2P) mixture in chloroform (20 mM) at different molar ratios (1 : 0, 3 : 1, 1 : 1, 1 : 3, 0 : 1). The first and second types of microemulsion was then combined and constantly stirred at ambient temperature for 1 h. Then 10 mL ethanol was added, followed by centrifugation at 10 000*g* for 15 min. This process was repeated three times and the obtained sedimentation layer was vacuum-dried to get the inorganic nano-core covered with the drug. The core particles were suspended in 500 μL of chloroform and mixed with 64.5 μL of cholesterol solution in chloroform (10 mg mL^{-1}), 46.5 μL of DOTAP solution in chloroform (25 mg mL^{-1}), 160 μL of DSPE-PEG 2000 (25 mg mL^{-1}) solution in chloroform. Afterwards, the organic phase was removed by rotary-evaporation and the obtained hybrid nanocarriers were dispersed in 400 μL of deionized water ready for use. The nanocarriers loaded with CPT-P and CPT-2P were abbreviated as LMnP-CPT-P and LMnP-CPT-2P, respectively.

Characterization of hybrid nanocarriers

The hydrodynamic diameters of different hybrid nanocarriers were determined using a Zetasizer Nano ZS (Malvern Instrument Ltd, Malvern, UK) at 25 °C (n = 3). The samples were diluted in deionized water (1 mg mL^{-1}) prior to dynamic light scattering (DLS) measurement. The morphology of hybrid nanocarriers was acquired using a Tecnai G2F20 transmission electron microscope (FEI, USA). The serum stability of different types of hybrid nanocarriers was measured by a fluorescence approach.[21] In brief, the hybrid nanocarriers were dissolved in fetal bovine serum (FBS) at a concentration of 200 μg mL^{-1}. The temperature was maintained at 37 °C. A FLS980 fluorescence spectrometer (Edinburgh Instruments Ltd) was employed to record the emission spectra (400–550 nm, slit widths: 1 nm) at 0 h, 0.5 h, 1 h, 2 h, 3 h, and 4 h post sample suspension in serum. The excitation wavelength of 369 nm was utilized with a slit width of 1 nm. At different time points, the maximum fluorescence intensity was divided by that at the starting point (0 h) and the corresponding ratios were plotted against time.

Determination of cargo loading in hybrid nanocarriers

The drug loading in the hybrid nanocarriers was quantified by high performance liquid chromatography (HPLC). A Dionex 3000 HPLC instrument was employed coupled with an ultraviolet (UV) detector and the detection wavelength was 369 nm. The elution was realized using a Waters Symmetry C18 column (250 mm × 4.6 mm, 5 μm) at 25 °C. The injection volume is 10 μL, and the mobile phase is a mixture of methanol and water (50% : 50%, v/v) containing 0.1% (v/v) acetic acid with a constant flow rate of 1 mL min^{-1}. Prior to the quantification, the nanocarriers (5 mg) were dissolved in a mixture of hydrochloric acid aqueous solution (1 M) and methanol (3 : 7, v/v), followed by sonication treatment to fully disassemble the nanocarrier. Then the obtained samples were diluted with the mobile phase before HPLC assay (n = 3). The content of Mn^{2+} in the nanocarriers was measured using a 180–80 polarized Zeeman atomic absorption spectrophotometer (AAS) (Hitachi High-Technologies Co. Ltd, Shanghai, China). In brief, LMnP-CPT-2P (*ca.* 5 mg) or the drug-free LMnP (*ca.* 2 mg) nanocarriers were dissolved in hydrochloric acid aqueous solution (37%, w/w). Sonication was applied for 1 h to completely damage the nanocarrier and liberate Mn^{2+}.

The obtained samples were diluted with deionized water (×10) prior to AAS quantification (n = 3).

In vitro CPT-2P and Mn^{2+} release

The release profile of CPT-2P and Mn^{2+} ions from the LMnP-CPT-2P nanocarriers (without inner DOPA lipid) was evaluated using a vertical Franz-type diffusion cell.[32] The receiver fluid was the phosphate-buffered saline at pH 7.4 (0.18 M) or citric acid–Na_2HPO_4 buffer at pH 5.0 (0.15 M). The nanocarriers (2.5 mg) were dispersed in the receiver fluid (2 mL); the donor and receptor compartments were separated by the regenerated cellulose membrane (MWCO = 3500 Da) with a total diffusion area of roughly 2 cm^2. The system was maintained at 37 °C using a waterbath (n = 3). At pre-determined time points (0.5, 1.0, 1.5, 2.0, 3.0, 4.0, 5.0, 6.0, 8.0, 10.0, 12.0, 24.0, and 36.0), 0.5 mL of receiver medium was withdrawn for HPLC analysis of drug concentration and the same volume of fresh receiver fluid was supplemented to keep the total volume of the receptor compartment constant (*ca.* 17 mL). The release of Mn^{2+} employed a similar approach; however, the receiver fluid contained additional EDTA (0.8 mM) to stabilize the released Mn^{2+}. The Mn^{2+} concentration was quantified using a 1.2 T HT/MRSI60-60KY MRI system from Huantong Corporation (Shanghai, China). The cumulative CPT or Mn^{2+} amount was plotted against time to obtain the release curve.

In vitro MRI analysis

LMnP-CPT-2P hybrid nanocarriers (4.26 mg) were dissolved in 10 mL of citric acid–Na_2HPO_4 aqueous buffers with different pH values (7.4, 6.0, and 5.0), which was used as the stock. The buffers also contained 0.8 mM EDTA. The stock suspension was diluted to achieve a series of Mn conditions (0.025 mM, 0.050 mM, 0.100 mM, 0.200 mM, and 0.400 mM). The T_1 spin–lattice relaxation time was recorded using a 1.2 T HT/MRSI60-60KY MRI system from Huantong Corporation (Shanghai, China). Then the r_1 relaxivity was obtained by calculating the slope of $1/T_1$-concentration curve (n = 3).

Cellular uptake and cytotoxicity analysis

Murine breast cancer cell line 4T1 was obtained from the state Key Laboratory of Medicinal Chemical Biology, Nankai University. The cells were cultured in DMEM medium (Logan City, Utah, USA), supplemented with 10% fetal bovine serum (Biolnd, Cromwell, USA), 100 U mL^{-1} penicillin, and 100 μg mL^{-1} streptomycin at 5% CO_2 and 37 °C. The cellular uptake of LMnP-CPT-2P hybrid nanocarriers was analyzed using a Leica TCS SP8 confocal laser scanning microscope (Leica Microsystems Inc., IL, USA). 4T1 cells were seeded in 35 mm plates at a density of 8×10^4 cells per well and incubated in DMEM at 37 °C for 24 h. Then, the culture medium was replaced with 1 mL of fresh medium containing free CPT, CPT-2P and LMnP-CPT-2P nanocarriers; the drug concentration was fixed at 10 μg mL^{-1}. After incubation for 4 h, cells were washed with PBS in triplicate and then fixed using 1 mL of paraformaldehyde (4%, w/v) for 20 min. The fluorescence images of the cells were obtained with the excitation wavelength at 405 nm and the emission wavelength at 420–500 nm. The cytotoxicity of LMnP-CPT-2P nanocarriers in 4T1 cells was assessed using the typical 3-(4,5-dimethylthiazol-2-yl)-2,5-diphenyl tetrazolium bromide (MTT) cell proliferation assay (n = 4). Free CPT and CPT-2P were used as controls. The cytotoxicity of the drug-free nanocarrier (LMnP) and $MnCl_2$ was also examined with the manganese dose matching that in LMnP-CPT-2P. In detail, the cells (4×10^3 per well) were incubated in 96-well plates for 24 h. Then five samples were supplemented with CPT dose at 0.5, 1, 2, 4, 6, 8, 10, 20, and 30 μM and the manganese dose was 1, 2, 4, 8, 12, 16, 19, 39, and 58 μM. After 48 h of incubation, the cells were thoroughly rinsed with PBS and then treated with MTT solutions (0.5 mg mL^{-1}) for another 4 h. Subsequently, the MTT medium was discarded and 100 μL of DMSO was added to each well. The optical density (OD) was measured on a Synergy 4 hybrid microplate reader (BioTek Instruments Inc., VT, USA) at 490 nm. The cell viability was calculated by the formula: cell viability (%) = $(OD_{sample}/OD_{control}) \times 100$, where OD_{sample} and $OD_{control}$ represent the OD values of the sample wells and the control wells. The half maximal inhibitory concentration (IC50) was calculated using the Origin software (OriginLab, Northsampton, MA, USA).

Hemocompatibility analysis

The hemocompatibility of hybrid nanocarriers was examined using a previously published method.[35] All animal experiments were performed in compliance with the guidelines set by Tianjin Committee of Use and Care of Laboratory Animals, and were approved by the Animal Ethics Committee of Tianjin University. The blood of female BALB/c mice (Vital River Laboratory Animal Technology Co. Ltd, Beijing China) was collected in heparinized tubes. The blood was mixed with 10 times of normal saline (0.9% NaCl, w/v). Afterwards, the suspension was centrifuged for 15 min (447 × g) at ambient temperature and the sedimentation layer was wahsed with normal saline three times. The pellets were diluted with normal saline in a ratio of 1 : 10 (v/v). The aliquots of obtained erythrocyte suspension (0.5 mL) were mixed with 0.5 mL of LMnP-CPT-2P nanocarrier aqueous suspension in normal saline (CPT: 150 μM; Mn^{2+}: 292 μM); the system was maintained at 37 °C. Similarly, the LMnP (Mn^{2+}: 292 μM) aqueous suspension and free CPT-2P (150 μM) controls were also treated with the same procedure with normal saline and deionized water used as the negative and positive controls, respectively. Three hours later, the samples were centrifuged (295 × g), followed by spectrophotometric assay of the supernatant at 540 nm in a Synergy 4 hybrid microplate reader (BioTek Instruments Inc., VT, USA). The degree of hemolysis was calculated and a value less than 2% was regarded as non-hemolytic (n = 3).

In vivo MRI and biodistribution analysis

BALB/c mice were inoculated subcutaneously (into the right flanks of mice back) with 4T1 cells (50 μL of 2×10^7 cells per mL). When the volumes of tumor reached *ca.* 50–100 mm^3, the mice were randomly divided into two groups (n = 3). LMnP-CPT-2P nanocarrier aqueous suspension (200 μL) was intravenously administered to the mice. The CPT and Mn^{2+} dose was 5 mg kg^{-1} and 1.5 mg kg^{-1}, respectively, based on animal weight.

$MnCl_2$ aqueous solution was used as the control with identical Mn^{2+} dose (1.5 mg kg^{-1}). At different time points post dose administration (0 h, 2 h, and 6 h), the whole animal was imaged using a 1.2 T HT/MRSI60-60KY MRI system from Huantong Corporation (Shanghai, China). The T_1-weighted imaging parameters are listed as follows: repetition time = 100 ms, echo time = 8.8 ms, field of view = 100 × 50 mm^2, matrix = 512 × 256, slice thickness = 1 mm, temperature = 20 °C. The contrast intensity of the region of interest in the tumor and normal regions were measured by the software and compared after normalization.

To investigate the biodistribution of LMnP-CPT-2P hybrid nanocarriers, a near infrared fluorescent probe (ICG) was incorporated into the core of the nanocarrier. Free ICG aqueous solution was the control. Both samples (200 μL) were intravenously injected to the 4T1 tumor-bearing mice. The ICG dose was maintained identical at 2 mg kg^{-1}. The kinetic fluorescence images of ICG were obtained at 2 h, 6 h, and 24 h post dose administration using a Cri Maestro *in vivo* imaging instrument (Cambridge Research & Instrumentation, Inc., MA, USA). The excitation wavelength was 735 nm and a 790 nm longpass emission filter was used. The background fluorescence signal was subtracted using the Maestro software. At 24 h post dose administration, mice were sacrificed, the major organs including the heart, liver, spleen, lungs, kidneys, and tumor were harvested for *ex vivo* imaging.

In vivo antitumor efficacy

The same 4T1 tumor-bearing mice were divided into four groups randomly (n = 6). Four samples (200 μL) including normal saline (the control group), CPT-2P (5 mg kg^{-1} of CPT), LMnP-CPT-2P nanocarrier (5 mg kg^{-1} CPT, 1.5 mg kg^{-1} Mn^{2+}), LMnP nanocarrier (1.5 mg kg^{-1} Mn^{2+}) were administered intravenously on the first, fourth and ninth day. The mice body weight and tumor volume were monitored every other day for each mouse. The tumor volume was calculated using the following equation: tumor size (mm^3) = (length × $width^2$/2). The relative tumor size was calculated by the tumor volume at a fixed time point against the initial tumor volume at the first day. After 16 days, all mice were sacrificed. The major organs as well as tumor tissues were collected and histologically evaluated using the standard hematoxylin and eosin (H&E) staining. The terminal deoxynucleotidyl transferase-mediated nick end labelling (TUNEL) assay was used to assess the degree of apoptosis and the procedure was in accordance with the supplier protocol (Promega Biotech Co., Ltd) (n = 3).

Statistical analysis

All data were expressed as mean ± standard deviation (SD). The statistically significant differences were identified and analyzed by Student's t test or one-way analysis of variance (ANOVA) accompanied by a Tukey's *post hoc* test at a minimal level of significance of 0.05.

Conflicts of interest

There are no conflicts to declare.

Acknowledgements

The work was financially supported by the National Natural Science Foundation of China (21650110447), the National Basic Research Program of China (2015CB856500), and the open fund of the State Key Laboratory of Medicinal Chemical Biology (Nankai University) (2017030).

References

1 Z. Cheng, Z. A. Al, J. Z. Hui, V. R. Muzykantov and A. Tsourkas, *Science*, 2012, **338**, 903.
2 X. Qian, Z. Gu and Y. Chen, *Mater. Horiz.*, 2017, **4**, 800.
3 V. P. Torchilin, *Nat. Rev. Drug Discovery*, 2014, **13**, 813.
4 R. Yang, S. Zhang, D. Kong, X. Gao, Y. Zhao and Z. Wang, *Pharm. Res.*, 2012, **29**, 3512.
5 C. Chen, R. Tao, D. Ding, D. Kong, A. Fan, Z. Wang and Y. Zhao, *Eur. J. Pharm. Sci.*, 2017, **107**, 16.
6 K. Park, *ACS Nano*, 2013, **7**, 7442.
7 T. Wei, C. Chen, J. Liu, C. Liu, P. Posocco, X. Liu, Q. Cheng, S. Huo, Z. Liang, M. Fermeglia, S. Pricl, X. J. Liang, P. Rocchi and L. Peng, *Proc. Natl. Acad. Sci. U. S. A.*, 2015, **112**, 2978.
8 K. Cai, X. He, Z. Song, Q. Yin, Y. Zhang, F. M. Uckun, C. Jiang and J. Cheng, *J. Am. Chem. Soc.*, 2015, **137**, 3458.
9 Y. Shen, E. Jin, B. Zhang, C. J. Murphy, M. Sui, J. Zhao, J. Wang, J. Tang, M. Fan, E. Van Kirk and W. J. Murdoch, *J. Am. Chem. Soc.*, 2010, **132**, 4259.
10 Z. Wang, C. Chen, Q. Zhang, M. Gao, J. Zhang, D. Kong and Y. Zhao, *Eur. J. Pharm. Biopharm.*, 2015, **90**, 53.
11 P. Huang, D. Wang, Y. Su, W. Huang, Y. Zhou, D. Cui, X. Zhu and D. Yan, *J. Am. Chem. Soc.*, 2014, **136**, 11748.
12 W. Gao, D. Lee, Z. Meng and T. Li, *J. Controlled Release*, 2017, **267**, 214.
13 D. Liu, H. Zhang, S. Cito, J. Fan, E. Makila, J. Salonen, J. Hirvonen, T. M. Sikanen, D. A. Weitz and H. A. Santos, *Nano Lett.*, 2017, **17**, 606.
14 C. P. Hollis, H. L. Weiss, M. Leggas, B. M. Evers, R. A. Gemeinhart and T. Li, *J. Controlled Release*, 2013, **172**, 12.
15 P. Mi, D. Kokuryo, H. Cabral, H. Wu, Y. Terada, T. Saga, I. Aoki, N. Nishiyama and K. Kataoka, *Nat. Nanotechnol.*, 2016, **11**, 724.
16 J. Li, Y. Yang and L. Huang, *J. Controlled Release*, 2012, **158**, 108.
17 K. Park, *J. Controlled Release*, 2015, **203**, 189.
18 R. Yang, S. Zhang, D. Kong, X. Gao, Y. Zhao and Z. Wang, *Pharm. Res.*, 2012, **29**, 3512.
19 T. Wei, C. Chen, J. Liu, C. Liu, P. Posocco, X. Liu, Q. Cheng, S. Huo, Z. Liang, M. Fermeglia, S. Pricl, X. J. Liang, P. Rocchi and L. Peng, *Proc. Natl. Acad. Sci. U. S. A.*, 2015, **112**, 2978.
20 K. Cai, X. He, Z. Song, Q. Yin, Y. Zhang, F. M. Uckun, C. Jiang and J. Cheng, *J. Am. Chem. Soc.*, 2015, **137**, 3458.
21 X. Dong, X. Guo, G. Liu, A. Fan, Z. Wang and Y. Zhao, *Chem. Commun.*, 2017, **53**, 3822.
22 M. Murakami, H. Cabral, Y. Matsumoto, S. Wu, M. R. Kano, T. Yamori, N. Nishiyama and K. Kataoka, *Sci. Transl. Med.*, 2011, **3**, 64ra2.

23 Y. Zhang, W. Y. Kim and L. Huang, *Biomaterials*, 2013, **34**, 3447.
24 B. Li, Z. Gu, N. Kurniawan, W. Chen and Z. P. Xu, *Adv. Mater.*, 2017, **29**, 29.
25 Y. Hao, C. Zheng, L. Wang, J. Zhang, X. Niu, Q. Song, Q. Feng, H. Zhao, L. Li, H. Zhang, Z. Zhang and Y. Zhang, *Acta Biomater.*, 2017, **62**, 293.
26 C. J. Choi, V. Anantharam, N. J. Saetveit, R. S. Houk, A. Kanthasamy and A. G. Kanthasamy, *Toxicol. Sci*, 2007, **98**, 495.
27 H. Yoon, D. S. Kim, G. H. Lee, K. W. Kim, H. R. Kim and H. J. Chae, *Environ. Health Toxicol.*, 2011, **26**, e2011017.
28 K. Xin, M. Li, D. Lu, X. Meng, J. Deng, D. Kong, D. Ding, Z. Wang and Y. Zhao, *ACS Appl. Mater. Interfaces*, 2017, **9**, 80.
29 H. Maeda, J. Wu, T. Sawa, Y. Matsumura and K. Hori, *J. Controlled Release*, 2000, **65**, 271.
30 E. Blanco, H. Shen and M. Ferrari, *Nat. Biotechnol.*, 2015, **33**, 941.
31 Y. Zhang, L. Peng, R. J. Mumper and L. Huang, *Biomaterials*, 2013, **34**, 8459.
32 X. Li, M. Gao, K. Xin, L. Zhang, D. Ding, D. Kong, Z. Wang, Y. Shi, F. Kiessling, T. Lammers, J. Cheng and Y. Zhao, *J. Controlled Release*, 2017, **260**, 12.
33 D. Peer, J. M. Karp, S. Hong, O. C. Farokhzad, R. Margalit and R. Langer, *Nat. Nanotechnol.*, 2007, **2**, 751.
34 S. Rietwyk and D. Peer, *ACS Nano*, 2017, **11**, 7572.
35 S. Liu, D. Lu, X. Wang, D. Ding, D. Kong, Z. Wang and Y. Zhao, *J. Mater. Chem. B*, 2017, **5**, 4918.